Surface & Coatings Technology 393 (2020) 125765

Contents lists available at ScienceDirect

Surface & Coatings Technology

journal homepage: www.elsevier.com/locate/surfcoat

Nondestructive measurement of mill-scale thickness on steel by terahertz time-of-flight tomography

Min Zhai[a,b], Alexandre Locquet[a,b,*], Cyrielle Roquelet[c], Patrice Alexandre[c], Laurence Daheron[c], D.S. Citrin[a,b]

[a] Georgia Tech-CNRS UMI2958, Georgia Tech Lorraine, 2 Rue Marconi, 57070 Metz, France
[b] School of Electrical and Computer Engineering, Georgia Institute of Technology, Atlanta, GA 30332-0250, USA
[c] ArcelorMittal Maizières Research SA, Voie Romaine, 57280 Maizières-lès-Metz, France

ARTICLE INFO

Keywords:
Nondestructive testing
Nondestructive evaluation
Terahertz imaging
Terahertz reflectometry
Oxide coatings
Coated metal

ABSTRACT

We measure in a nondestructive and noncontact fashion the thicknesses of three scale films with thicknesses 28.5 ± 1.4 μm, 13.4 ± 0.9 μm, and 5.1 ± 0.3 μm on steel substrates employing terahertz time-of-flight tomography combined with advanced signal-processing techniques. Wüstite is the dominant phase in the scale films, though magnetite and hematite are also present. Because wüstite is electrically insulating, the incident terahertz electromagnetic pulses largely penetrate into the scale film; however, the pulses are entirely reflected by the underlying electrically conductive steel substrate. Because the film layers are thin, in some cases optically thin, the distinct pulses reflected at the air/scale and scale/steel interfaces overlap in time and thus are not visually evident in the reflected terahertz signal, necessitating the use of deconvolution techniques to recover the sample structure. We compare the merits of three deconvolution techniques, one unsuccessful (frequency-wavelet domain deconvolution) and two successful (sparse deconvolution and autoregressive extrapolation), to characterize the thicknesses of these scale films.

1. Introduction

MILL SCALE is a mixture of iron oxides [iron (II) oxide FeO (wüstite), iron (III) oxide Fe_2O_3 (hematite), and iron (II,III) oxide Fe_3O_4 (magnetite)] that forms on steel during the hot-rolling process. Wüstite in particular is a relatively uncommon phase but may be the dominant constituent of scale at early times before this metastable phase decays into other iron oxides. At room temperature, wüstite is electrically insulating; hematite is also insulating, though magnetite is conducting. In the manufacturing process of rolled steel, tertiary mill scale may be desirable to suppress surface corrosion, but later, when the steel is to be finished, the presence of mill scale may inhibit adhesion of coatings. Scale is thus typically removed prior to coating through acid pickling or other techniques. Being able to determine in a nondestructive and noncontact way the thickness of the scale layer is useful to optimize the pickling process as well as other production processes related to steel manufacturing. The determination of mill-scale thickness is typically carried out by destructive testing. This is slow and expensive, and requires interrupting the production and/or shipment of the steel to cut coupons to be tested. If the scale is not fully removed due to insufficient pickling, subsequent coating adhesion may be severely compromised. If pickling is too aggressive, excess toxic material may be generated along with higher energy costs. In this paper, we demonstrate that terahertz (THz) electromagnetic techniques in conjunction with advanced signal processing can be used to measure scale thickness down to ~5 μm on steel plate in a nondestructive and noncontact fashion. The success of the approach relies on the application of advance signal-processing techniques that enable the reconstruction of the film thickness even when below the naïve axial resolution limit of the experiment.

In a larger context, nondestructive techniques for characterizing and monitoring coatings on metal are important to ascertain coating uniformity and monitor surface processes. The conventional approach to obtain the layer structure employs destructive techniques based on metrology of micro-sample cross sections taken from the objects, which are not only destructive, but time consuming. Moreover, such thickness measurements are limited to the cross section itself. Clearly, nondestructive approaches are often more attractive. To date, various nondestructive-evaluation (NDE) techniques have been explored to study the structure and condition of coatings on metals, such as electrochemical impedance spectroscopy (EIS) [1], scanning electrochemical microscopy [2], acoustic emission [3], thermography and eddy-current testing [4]; however, not all of the techniques are capable

* Corresponding author at: Georgia Tech-CNRS UMI2958, Georgia Tech Lorraine, 2 Rue Marconi, 57070 Metz, France.
E-mail address: alocquet@georgiatech-metz.fr (A. Locquet).

https://doi.org/10.1016/j.surfcoat.2020.125765
Received 26 August 2019; Received in revised form 3 April 2020; Accepted 10 April 2020
Available online 13 April 2020
0257-8972/

of providing *quantitative* information in depth such as the layer thickness. Approaches such as scanning acoustic microscopy [5] and laser ultrasonic imaging [6] suffer from high attenuation at the requisite high frequencies which limits the penetration of ultrasound waves into the sample. Specifically, with regard to monitoring mill scale, for THz techniques to be helpful, it may be necessary to carry out the measurement when the steel is at elevated temperature, before the scale transitions to more electrically conducting phases, necessitating techniques that can be applied at some standoff distance. Therefore, alternative NDE techniques with relative high resolution, sufficiently low attenuation, and without contact are essential for numerous tasks related to evaluating coating thickness and condition.

Due to the ability of THz electromagnetic radiation to penetrate significantly into many electrically insulating materials, THz reflectometry has attracted considerable attention to provide information at quantitative depth in a nondestructive fashion. One study has been carried out to measure iron-oxide film thickness on steel using THz reflectometry [7]. That work focused on presumably polycrystalline hematite films and wüstite/magnetite bilayer films on steel. Pulsed THz reflectometry was carried out. The THz pulses covered the frequency range from 200 GHz to 1.4 THz. For hematite films (insulating) of thicknesses ranging from 11.5 to 20 μm, the amplitude reflectance data (square-root of power spectrum of the reflected signal) shows fringes in the frequency domain; the Fabry-Perot fringe spacing together with a knowledge of the refractive index of hematite (~5.5 obtained from separate THz transmission experiments) was used to obtain the film thickness. Note that the Fabry-Perot effects equivalent to using the time-delay between reflected pulses from the air/film and film/substrate interfaces (time-of-flight technique; see below).

Next in Ref. [7], magnetite films were studied. As magnetite has a significant conductivity, the THz penetration is insignificant on the thickness scale of the films. Instead, films were annealed thus converting most of the film to wüstite leaving behind a ~1-μm thick magnetite layer between the wüstite and steel substrate. The resulting wüstite films in Ref. [7] were of thickness 5, 10, and 15 μm. The thickness of the wüstite films were then measured by THz reflectometry and the amplitude reflectance spectra were fit to theoretical spectra to extract film thickness. Note that the amplitude reflectance spectrum does not exhibit obvious fringes, but presumably due to the increase in attenuation with increased film thickness, the overall reflectance depends on film thickness. Note that (1) the measurement required the films to the annealed to result in wüstite and (2) the results needed to be calibrated against theoretical reflectance spectra.

In the present paper, we apply THz time-of-flight (TOF) tomography in reflection mode to characterize the thickness of multiphase films resembling mill scale. In our work, the films need not be annealed to carry out the thickness measurement. In addition, we do not require a detailed knowledge of the THz attenuation of the multiphase film. Heuristically, the depth information may be obtained using THz TOF tomography by analyzing the various reflected THz signals we call *echoes* that occur at interfaces between materials with different refractive indices as determined by the respective Fresnel coefficients. The time delays between these echoes in conjunction with a knowledge of the refractive indices can be used to obtain the thicknesses of the layers. THz TOF tomography to characterize thin layers has been employed to measure the stratigraphy of systems as diverse as art paintings [8], dental tissue [9], automotive paints [10], and metal films [11]. Some of the results presented here were reported in summary form in Ref. [12].

The above procedure, which ultimately relies on the Fabry-Perot effect, works well provided the time delays between echoes exceed the duration of the THz pulse employed to interrogate the sample, i.e., for optically thick coatings. It is for this reason, the approach is often called the time-of-flight technique. If, however, the time delays are comparable to or less than the pulse duration, the various echoes may overlap temporally and not be obvious in the raw reflected signal. To extract the depth information that may be hidden in the overlapping echoes, deconvolution techniques are employed to distinguish the various closely spaced echoes that contribute to the reflected signal. Indeed, in general the recorded reflected signal is the convolution of the incident THz pulse and the impulse-response function $h(t)$ of the sample, which is independent of the incident pulse (also called the *reference pulse*) used; $h(t)$ gives the reflected signal one would expect given a δ-function incident pulse. The impulse-response function $h(t)$ determines the electric field of the reflected signal $r(t)$ given the electric field of the reference signal $i(t)$ via the convolution

$$r(t) = \int_{-\infty}^{\infty} h(\tau) i(\tau - t) d\tau.$$

By exploiting *prior* information we have about the sample (such as it is a layered structure or by assuming that the reflected signal is in an information-theoretic sense simple), in some cases deconvolution techniques may yield subwavelength information in the axial direction; such approaches have shown great potential to disentangle the overlapping echoes and to characterize the layer structure [13]. Various deconvolution techniques have been employed in the context of THz reflectometry, and the choice depends on the sample type and how the layer thickness compares with the minimum wavelength within the usable pulse bandwidth. For example, THz frequency-wavelet domain deconvolution (FWDD) and its variants have been applied reliably to reconstruct $h(t)$ for cases in which the layer thicknesses are similar to half the minimum wavelength in the medium within the pulse bandwidth [14–16]. As we discuss below, FWDD essentially uses filtering together with a linear basis transformation to reconstruct $h(t)$. As such, FWDD is resolution limited in the axial direction. In this work, we apply two further alternative postprocessing techniques that hold the promise of significantly enhanced axial resolution and/or dynamic range. After showing that FWDD is not successful in recovering the film thicknesses, we apply sparse deconvolution (SD) and autoregressive (AR) spectral extrapolation.

SD as implemented in Refs. [17–19] is a pure time-domain technique that can provide a more accurate reconstruction of the impulse response function $h(t)$ in which several sharp peaks associated with discrete interfaces lie on a zero background; AR, on the other hand, extrapolates the spectrum exploiting assumptions about the complexity of the signal into the low signal-to-noise (SNR) frequency regions based on the spectrum in the high-SNR band.

In this paper, we successively apply these techniques in an attempt to determine the thickness of scale films of controlled thickness on steel. The scale films are produced synthetically and are expected to be primarily wüstite as discussed below. In the following, we consider three successively thinner scale films, viz. of thicknesses 28.5 ± 1.4 μm, 13.4 ± 0.9 μm, and 5.1 ± 0.3 μm on steel substrates (as determined independently by destructive characterization) placing increasing demands on the deconvolution technique. Film thicknesses are recovered successfully, nondestructively, and without contact by means of THz TOF tomography combined with deconvolution. We further evaluate the limits of SD and AR for this type of sample and our experimental setup.

2. Sample and experiment

The samples are shown in Fig. 1. The films consist of a single scale layer grown under controlled conditions on interstitial-free steel substrates. Three scale films with thickness 28.5 ± 1.4 μm, 13.4 ± 0.9 μm, and 5.1 ± 0.3 μm are investigated. Destructive measurements of the cross sections, based on optical microscopy, were carried out independently to estimate film thicknesses, which are not uniform across the disks, and are reflected by the ranges of values given. The scale films were fabricated under an atmosphere of 20.9% oxygen and 15% water vapor. The growth duration and temperature were 2 min at 600 °C for the film of thickness 28.5 ± 1.4 μm, 4 min at 650 °C for the

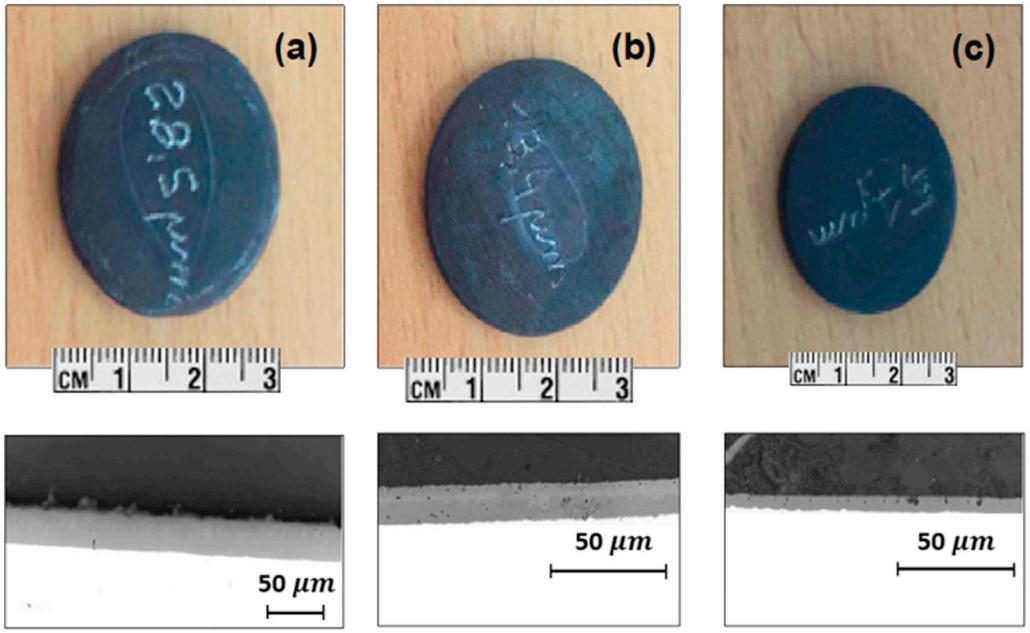

Fig. 1. Optical photographs of the three scale films of thickness (a) 28.5 ± 1.4 μm, (b) 13.4 ± 0.9 μm, and (c) 5.1 ± 0.3 μm on steel substrates. The steel disks are approximately 3 cm in diameter for all samples. Lower panels show cross-sectional optical micrographs through the samples.

thickness 13.4 ± 0.9 μm, and 3.5 min at 750 °C for the thickness 5.1 ± 0.3 μm. The procedure for surface preparation before scale growth is proceeded by cleaning with ethanol and then light manual polishing at 800 °C for a few seconds to remove any lubricant and hydroxide residue due to preparation and storage. Scale is composed predominantly of three different iron oxides: wüstite, hematite, and magnetite. Wüstite is the mineral name of iron (II) oxide; magnetite corresponds to iron (II, III) oxide and hematite to iron (III) oxide. Wüstite is an unstable phase that in atmosphere undergoes a reaction over the course of weeks to months, depending on temperature and humidity, resulting in magnetite [20]. Wüstite is a poor electrical conductor at 1 THz [21] permitting the incident THz wave to propagate within the material, as is hematite, whereas magnetite is quite conductive and thus less prone to be characterizable at depth by means of THz reflectometry. Note that good electrical conductors have high THz reflectivity; THz waves will not significantly penetrate good conductors, such as the underlying steel.

After the THz measurements, the composition of the films was verified by x-ray diffraction (XRD) (D2 Advanced X-ray Diffractometer, Bruker, Germany) in the 2θ range of 10–80° and scanned with 300 W Co anode radiation produced by a ceramic x-ray tube. The x-ray diffractograms of the 28.5 ± 1.4 μm thick film is shown in Fig. 2. Evidence of wüstite as well as other iron-oxide phases is present in the x-ray diffractogram. The presence of magnetite and hematite peaks is expected due to the instability of wüstite, and the relative intensities of the peaks are indicative of the concentrations of each iron oxide in the sample. Based on the Rietveld refinement principle, through adjusting the crystallographic parameters and the proportions of each phase so as to create the simulated diffractogram closest to the experimental diffractogram, the content of each indexed phase in this sample could be estimated, as presented in Fig. 3. It shows that the wüstite is the dominant phase (58% by mass) in the scale films.

The THz optical constants of wüstite, magnetite, and hematite are not very well established and values show considerable scatter. A useful resource of relevant references is nonetheless found in Ref. [22]; however, data are rather incomplete, covering powdered as well as single- and poly-crystalline samples and with data in the desired frequency band sparse. The THz refractive index of wüstite is given as 4.7 in Ref. [23]; that of hematite as ~5.5 in Ref. [22]. In Ref. [24] the THz real refractive index of single-crystal hematite is between 4 and 4.4 depending on crystal orientation. Magnetite is a conductive but minority phase, so that its presence will mainly attenuate the THz signal as it propagates through the film. The THz real refractive index of magnetite may be as high as 8.25 [24]. Büchenau and Müller, however, find a far-infrared refractive index of ~2.8 [25]. The comparison is shown graphically in Ref. [26]. Nonetheless, as the real refractive indices for wüstite and hematite oxides may be close, we shall assume the value $n = 4.7$ for the films. This value turns out to be in quite consistent with the experimental results.

The THz experiments were carried out in an air-conditioned laboratory at 22 °C with humidity < 48%. Otherwise, the samples were stored in a dry box to retard the transformation of wüstite from transforming into magnetite. The experiments shown here were conducted within the 3 months of sample fabrication to ensure that the scale films were primarily composed of wüstite. The THz reflection measurements are taken on a TeraView TPS Spectra 3000, a pulsed, broadband THz time-domain spectroscopy (TDS) system, shown in Fig. 4. The pulse duration is ~2 ps while the spectral bandwidth extends from ~100 GHz to 3 THz. (Note, however, that not all this bandwidth, particularly at the high-frequency end, is useful in our experiments, since the reflected pulse is significantly attenuated with respect to the incident pulse causing part of the pulse bandwidth at high frequency to fall below the noise floor.) The reference pulse produced by the apparatus shown in Fig. 5 was recorded by setting a bare metal plate (i.e., an excellent THz reflector) at the sample position. In particular, numerous water-vapor absorption lines are evident in the spectrum. The influence of water-vapor absorption can be eliminated by conducting measurements in dry nitrogen or via various denoising techniques. The basic experiment is described in detail in Ref. [27].

Once the reference pulse was characterized, we proceeded with THz TOF tomography. The samples were raster-scanned by a set of motorized stages moving in the transverse x and y directions in 100 μm steps over the entire sample. (Due to the spectral bandwidth and the relatively high numerical aperture of the THz optics, transverse resolution is limited to ~300 μm.) The data sampling period in this measurement is set to $T_s = 0.0116$ ps. Each recorded reflected temporal THz waveform contains 4096 data points, and the signal is averaged over 10 shots per pixels. For this sampling rate, the entire frequency spectrum

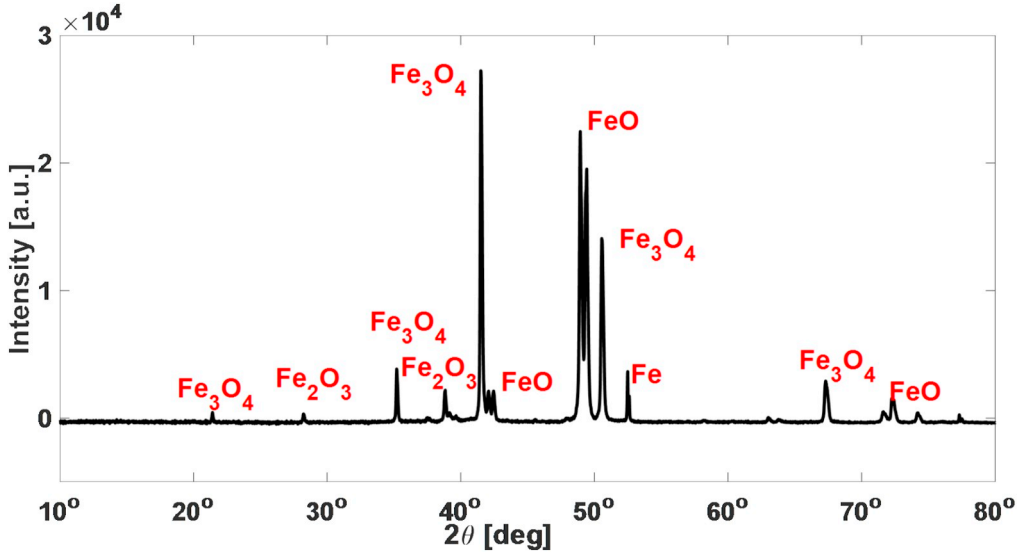

Fig. 2. X-ray diffractogram of 28.5 ± 1.4 μm thick sample. Diffraction lines associated with various iron-oxide phases are indicated.

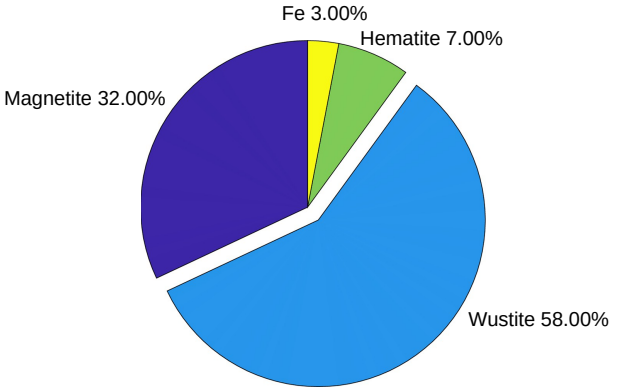

Fig. 3. Estimated proportion of various iron oxides in the 28.5 ± 1.4 μm sample based on XRD data (see Fig. 2).

obtained by a fast Fourier transform is from 0 to 85.99 THz, which contains 4096 data points.

3. Results and discussion

The reflected THz signals as received (the *raw* signals) from the samples with various film thicknesses are shown in Fig. 6(a)-(c). The shapes of the reflected THz signals are superficially similar to the reference THz signal shown in Fig. 5. The echoes off the air/scale and scale/steel interfaces temporally overlap and are not visually distinguishable in the raw reflected signals for any of the three samples. [The impulse response function $h(t)$ governing the measurement, as discussed above, relates the reflected THz signal $r(t)$ to the reference THz pulse $i(t)$. In the ideal case that the reference is an impulse, $\delta(t)$, the reflected signal would be $h(t)$.] In order to reconstruct the impulse response function $h(t)$ and thus reveal the structural properties of the samples, a standard frequency-domain approach, THz FWDD, is first attempted at each pixel [15]. The approach is described in detail in Ref. [28]. The idea is to reconstruct the transfer function $H(f)$ with f the frequency [Fourier transform of the impulse response function $h(t)$; lower case letters with argument t stand for time-dependent functions; upper case letters with argument f stand for their respective Fourier transform and are functions of frequency f] ideally as $H(f) = R(f)/I(f)$, where $R(f)$ and $I(f)$ are the Fourier transforms of $r(t)$ and $i(t)$, respectively. The problem is that in frequency ranges where noise dominates, this ratio is subject to substantial error.

We implement FWDD after first low-pass filtering to eliminate spurious spikes in the high-frequency region; FWDD itself corresponds to projecting the filtered signal onto a truncated basis of wavelets chosen to resemble the THz pulse $i(t)$, and thus improves the SNR by wavelet denoising. In other words, FWDD is a filter specially chosen to pass features resembling $i(t)$. Finally, $h(t)$ is reconstructed by taking the

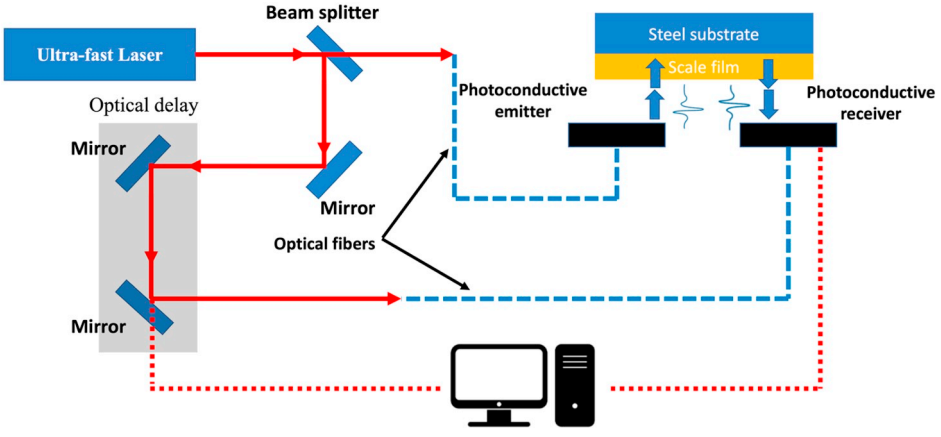

Fig. 4. Schematic diagram of the THz TDS system.

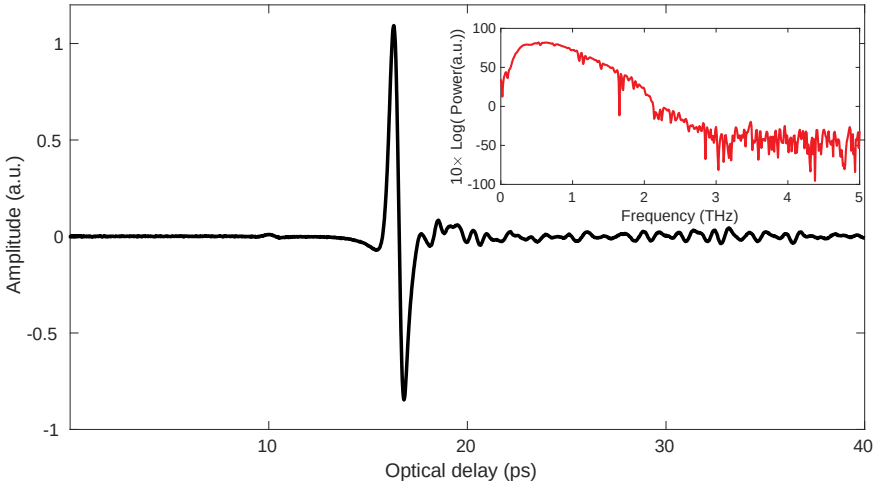

Fig. 5. THz signal (reference signal) $i(t)$ produced by the system with its frequency spectrum (inset). Reference data is obtained by placing a bare steel plate (good electrical conductor) at the sample location.

inverse Fourier transform of the transfer function $H(f)$ obtained by the procedure described above.

We first discuss the low-pass filter applied prior to FWDD itself. A Hanning window function is chosen as the filter function

$$F(\omega) = \begin{cases} e^{i\omega t_0} cos^2\left(\frac{\omega}{4f_c}\right), & |\omega| \le 2\pi f_c \\ 0, & |\omega| > 2\pi f_c \end{cases}$$

where t_0 is the arrival time of the main peak in time domain; $t_0 = 16.25$ ps is chosen for these scale films. The cutoff frequency $f_c = 3.5$ THz is chosen to suppress the low-SNR band of the reference and reflected signals as shown in Fig. 7. Due to the THz bandwidth generated by TPS spectra 3000 (60 GHz to 3 THz), we find that if f_c is lower that 3 THz, some weak though valuable features in the signals would be treated as system noise, and be eliminated by frequency-domain filter; if f_c is larger than 4 THz, residual background noise in frequency-domain blurs the valuable information in the time and frequency domains. For wavelet denoising, *symlet* (sym4) wavelets were used with decomposition level equal to 7 [9]; no significant improvement is achieved with higher depth to justify the extra computational expense. The estimated impulse responses $h(t)$ when applying FWDD are shown in Fig. 6(d)-(f). While the 28.5 μm film might nominally be within the axial resolution limit of FWDD, attenuation (reducing the amplitude of the echo from the back scale/steel interface) reduce the usable THz bandwidth so that the high-frequency part of the detected spectrum lies below the noise floor. We therefore conclude that FWDD is not successful even on the thickest film studied here. Because the wavelet basis chosen is well suited to the reference pulse, it is not likely a different basis (or a different filter) will likely not improve the situation.

Next, in order to attempt to reconstruct the layer structure, SD [19,29] is applied to analyze these samples. SD is a time-domain approach to reconstruct $h(t)$. Heuristically, SD works as summarized in the next few paragraphs. The impulse response functions $h(t)$ for layered structures are a class of signal comprised of a limited number of discrete echoes associated with a reflection from each material interface (multiple echoes are typically too weak to be of importance) on an otherwise

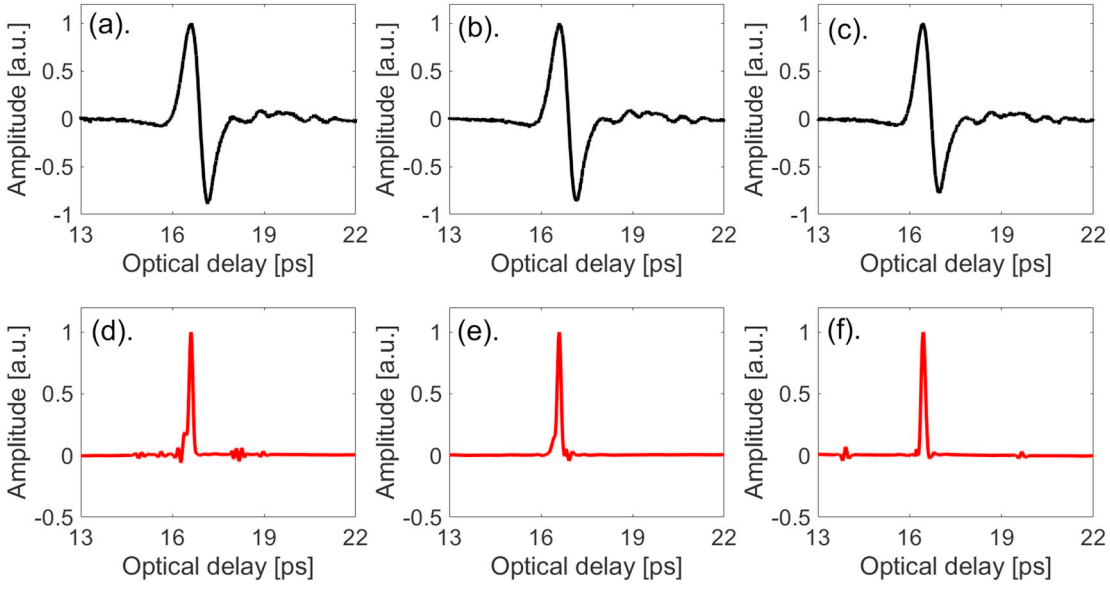

Fig. 6. The raw reflected THz signal $r(t)$ [(a)-(c)] and the impulse-response function $h(t)$ reconstructed by FWDD [(d)-(f)] for scale films with thicknesses 28.5 ± 1.4 μm, 13.4 ± 0.9 μm, and 5.1 ± 0.3 μm. © 2019 IEEE.
Reprinted with permission from Ref. [12] M. Zhai, A. Locquet, C. Roquelet, and D. S. Citrin, Terahertz non-destructive thickness characterization of optically thin scale layers on steel, 44th International Conference on Infrared, Millimeter, and Terahertz Waves 2019, https://doi.org/10.1109/IRMMW-THz.2019.8874181.

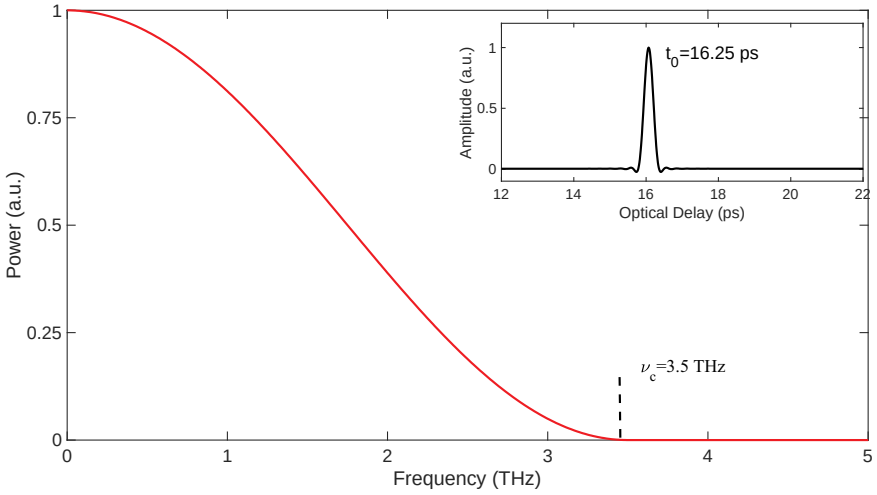

Fig. 7. Hanning window function in time domain with $t_0 = 16.25$ ps and $f_c = 3.5$ THz, and its Fourier transform in the inset.

signal-free background; therefore, $h(t)$ has a *sparse* representation (it will be a sequence of sharp peaks on a zero background), which means that only a limited number of data points have nonzero values. By exploiting the sparse constraint, the algorithm focuses on the detection of interfaces and can be expected to lead to a better dynamic range than the FWDD technique. For the SD reconstruction of $h(t)$, the convolution matrix is formed by the experimentally obtained reference THz signal, which contains 4096 data points, and the iteration is performed 3000 times. Details can be found in Ref. [19].

In the SD algorithm, a parameter λ controls the amplitude of the regularization. Moreover, the energy is minimized by iterative thresholding. In the case of soft-thresholding employed here, the step size τ should obey

$$\tau < \frac{2}{\|H^{\mathrm{T}}H\|_2}.$$

Considering the SNR and the tradeoff between the sparsity of the impulse response function $h(t)$ and the residue norm, the regulation parameter $\lambda = 0.8$ and the value of the step size τ is set to $1.5/\|H^{\mathrm{T}}H\|_2$. We checked that similar results were obtained consistently for λ and τ. Balancing between the accuracy of result and the computational time, the number of iterations is selected to be 3000.

The corresponding deconvolved signals are shown in Fig. 8(d)-(f). Whereas distinct echoes are not visually evident in the raw THz reflected data in Fig. 8(a)-(c), in the SD reconstructions of $h(t)$, two pronounced echoes can be identified clearly for all the samples. In order to visualize the origin of the two peaks in $h(t)$ a schematic diagram of the sample cross section is shown in Fig. 9. The first echooriginates from the air/scale interface while the temporally second echo is due to the scale/steel interface. Multiple reflections are expected to be weak and are thus not identified in the SD reconstruction of $h(t)$. The optical thickness of the coating can be calculated from the time delay between the first and second peak in the reconstructed $h(t)$ and the refractive index of scale. The delay between the first and second echoes for the 28.5 μm, 13.4 μm, and 5.1 μm films is 0.9 ps, 0.4 ps, and 0.16 ps, respectively. The physical thickness of the film is obtained from

$$L_{layer} = \frac{\Delta t}{2}\frac{c}{n}$$

where c is the *in-vacuo* speed of light, Δt is the time delay between the first and second echoes, the factor $1/2$ arises since the THz pass through the film twice in the reflection geometry [30], and n is the refractive

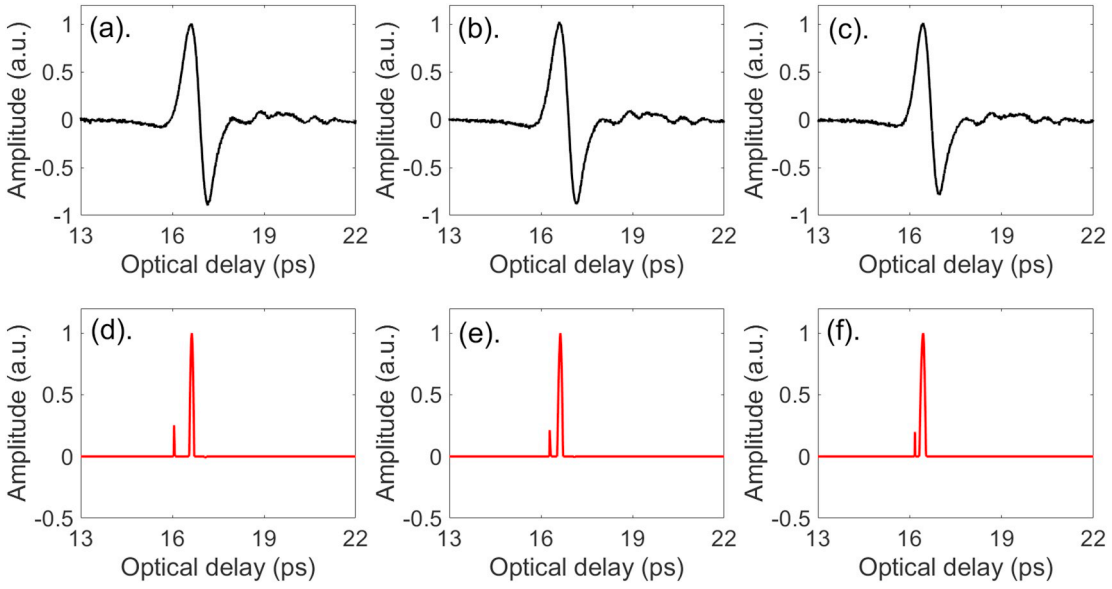

Fig. 8. The raw reflected THz signal $r(t)$ [(a)-(c)] and SD-reconstructed impulse response function $h(t)$ signal [(d)-(f)] for films of thickness 28.5 ± 1.4 μm, 13.4 ± 0.9 μm, and 5.1 ± 0.3 μm.

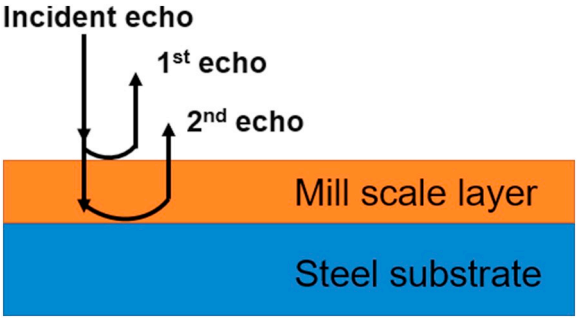

Fig. 9. Schematic diagram of sample cross section. Arrows indicate the dominant echoes contributing to the peaks in the impulse response function $h(t)$. Note that multiple reflections, which in practice here are quite weak, are not shown or revealed in the reconstructed impulse response function $h(t)$.

Table I
Comparison of calculated thickness from SD and AR with destructive metrology of micro-sample cross sections. The mean and standard deviation of scale thickness is obtained from 20 different pixels for each sample.

Thickness (μm)	Mean of SD (μm)	STD of SD (μm)	Mean of AR (μm)	STD of AR (μm)	Mean of cross-section (μm)	STD of cross-section (μm)
28.5	28.1	0.6	28.05	0.82	28.5	1.4
13.4	12.8	0.63	13.3	0.52	13.4	0.9
5.1	6.6	0.41	5.7	0.39	5.1	0.3

index of wüstite, since this was determined above to be the dominant phase in the scale. The zero-frequency refractive index of scale is close to 4.7, as discussed above [23]. In turn, the SD-reconstructed physical film thicknesses are estimated, for a given pixel, to be 28.4 μm, 12.8 μm, and 9.6 μm, as summarized in Table I, which are close to the independently measured ranges of values 28.5 ± 1.4 μm, 13.4 ± 0.9 μm, and 5.1 ± 0.3 μm obtained by destructive cross-sectional measurement. In particular, the two thicker films are within the thickness variation across the samples of the nominal thicknesses. These results indicate that SD is an effective approach to obtain the structural properties for the two thicker films. SD, however, appears to fail to provide a high-quality estimate of the thickness of the 5.1 μm film for the explored parameter ranges. Basically, SD cannot distinguish multiple echoes if the SNR is too low, if the echoes are too close and/or if the sampling time is too long. In addition, dispersion in the optical constants results in pulse spreading [31], which may degrade the accuracy and axial resolution for SD, though is not likely to be an issue with thin films.

Since SD was not successful in providing a high-quality reconstruction of $h(t)$ for the thinnest film, we resort to another technique, AR extrapolation [10], which extends the exploitable spectral bandwidth and can be expected to lead to a higher axial resolution. The procedure works as follows. We first obtain $H(f)$ in the frequency band where SNR is high from the experimental data as the ratio $R(f)/I(f)$. In our case, the information we will exploit is that for layers on a reflective substrate, we expect the transfer function $H(f)$ to be a sinusoid due to the Fabry-Perot effect. Lastly, the reconstructed $H(f)$ is inverse Fourier transformed to obtain $h(t)$ and the time delays between peaks are used to determine the relevant optical delays and in turn the film thickness.

Unlike FWDD, which discards information as a consequence of filtering, namely the frequency components in the low-SNR regions in order to suppress anomalous spikes that would otherwise appear in $H(f)$, AR deconvolution aims at *reconstructing* the missing frequency components in precisely the low-SNR regions. That is, FWDD relies on frequency filtering, whereas AR seeks to estimate missing frequency information. In an AR process, each data point H_i is modeled as a weighted sum of its previous p points as well as a noise term N_i,

$$H_i = \sum_{k=1}^{p} a_k H_{i-k} + N_i,\ i > p$$

$$H_i = \sum_{k=1}^{p} b_k H_{i+k} + N_i,\ i < p$$

where p is the order of AR process and a_k and $b_k$is a parameter of the AR model. The AR model is fitted using a limited window of frequencies with high SNR, and used to predict the unknown value outsides the window range. For the data corresponding to larger frequencies than those of the window region, a forward prediction filter can be applied, while for lower frequencies, a backward prediction filter is applied. Considering the THz bandwidth and the SNR of our TDS system, we fit the AR model to the experimental data within a frequency window with low-cutoff frequency $i_L = 0.15$ THz and high-cutoff frequency $i_H = 2$ THz. The reason the frequency band 0.15 THz to 2 THz is selected is to focus on the high-SNR region compared with the residual low-SNR region, enabling us to reliably extrapolate the signal into the low-SNR region. In practice, the high-SNR band i_L to i_H is divided into three subintervals: one interval is used to derive to the backward coefficient, one interval is used as the base of AR model, and the last interval is used to derive to the forward coefficient. The AR coefficients are obtained by minimizing the sum of the forward and backward prediction error ${\epsilon_p}^2$, which is expressed as

$$\epsilon_p^2 = \sum_{i=i_L}^{i_{PL}} \left| H_i - \sum_{k=1}^{p} b_k H_{i+k} \right|^2 + \sum_{i=i_{PH}}^{i_H} \left| H_i - \sum_{k=1}^{p} a_k H_{i-k} \right|^2$$

where i_{PL} to i_{PH} is the frequency range that serves as the base for AR model, a_k and b_k are the forward and backward coefficients, respectively, and H_i is the data point within the window i_L to i_H.

The approach for selecting the order p of the model is based on Akaike's information criterion (AIC) [32], which can be calculated using ${\epsilon_p}^2$,

$$(AIC)_p = N \ln(\epsilon_p^2) + 2p.$$

Akaike's criterion leads to an estimated order of $p = 56$. Hence, data within the range 0.15 THz to 0.25 THz are used to find the coefficient for the backward prediction filter; data within 1.43 THz to 2 THz are used to find the coefficient for the forward prediction filter.

Using the AR model as a prediction filter, the missing data in the regions below 0.15 THz and above 2 THz can be extrapolated clearly for all samples. The echo from the scale/steel interface can also be seen clearly. We find that the axial resolution of AR is higher than SD and, we shall see, reliably provides the film thickness, even for the thinnest film. This is consistent with our previous work [33] that has found that AR can be more effective than SD for single-layer structures. The deconvolved signal based on the reconstructed transfer function $H(f)$ can also be compared with the spectra of the raw reflected signals, as shown in Fig. 10(d)-(f). Due to the estimation and recovery of the frequency components throughout the entire spectrum, the second echo, corresponding to the scale/steel interface is also identified in all cases. We observe that the calculated thickness based on the optical delay between the two positive echoes matches well with the nominal thickness 5.1 ± 0.3 μm. The mean and standard deviation for 20 pixels selected at random from the nominal 28.5 μm, 13.4 μm, and 5.1 μm films are found to be 28.05 ± 0.82 μm, 13.3 ± 0.52 μm, and 5.7 ± 0.39 μm, respectively.

To estimate the uniformity of the THz-based measurement of the films, 20 pixels associated with various spatial positions on the samples for each film are selected randomly, the minimum distance between each measured pixel is ~500 μm. The reflected THz signals at those pixels are recorded. Through measuring the optical delay between the first and second positive echoes, the thickness of film at that pixel can be calculated with the equation mentioned above. The mean and standard deviation for those 20 pixels for each film is obtained. Table I

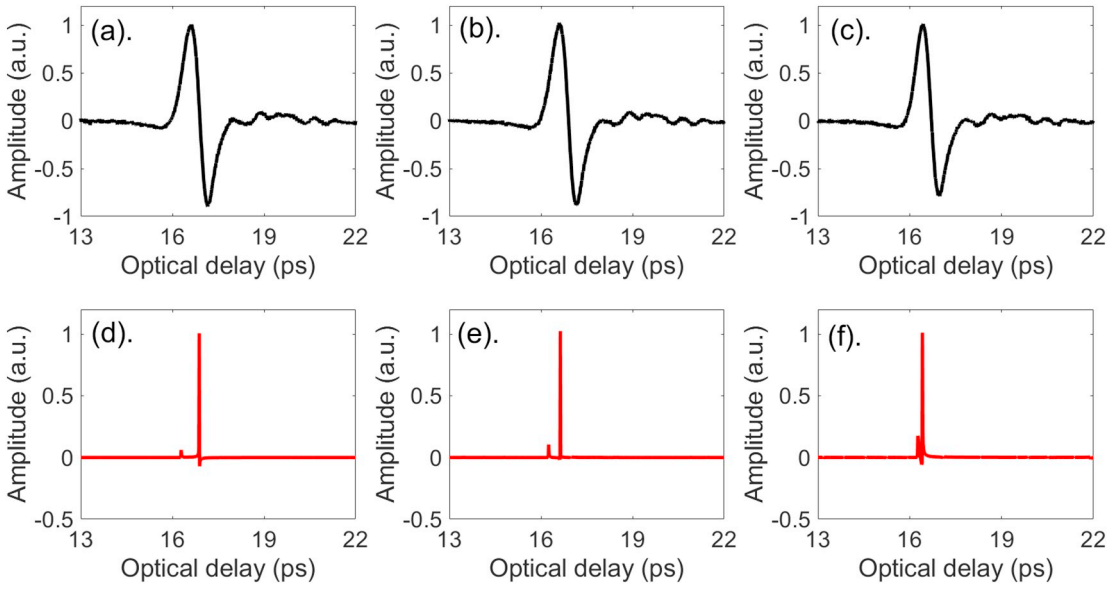

Fig. 10. Deconvolution results based on AR and the raw THz signal reflected from the calamine sample: 28.5 ± 1.4 μm, 13.4 ± 0.9 μm, and 5.1 ± 0.3 μm, respectively. (d)-(f). Estimated frequency spectrum (up to 5 THz) based on the AR method for each sample.

shows the calculated scale film thickness based on AR for nominal 28.5 μm, 13.4 μm, and 5.1 μm matching fairly well with the cross-sectional measurements. In addition, Table I summarizes all the results for SD as well. Hence, we conclude that the axial resolution in this single-layer film is significantly enhanced by AR deconvolution, and the structural properties of scale films with thickness down to ~5 μm can be resolved by AR deconvolution. (We also note that not shown here, we were successful in applying AR on a 4-μm thick scale film.) Of note, the cross-section method only gives the thickness along the cross-section; the film thickness was thus estimated based on the assumption that the entire film is uniform in thickness. The AR result, on the contrary, enables one to explore uniformity across a surface. This is a further advantage of the THz approach versus traditional destructive cross-sectional measurements.

4. Conclusion

In this paper, THz reflectometry together with two different deconvolution techniques, namely SD and AR, are presented to analyze the thickness of single-layer scale films on steel substrates. These are multiphase films with wüstite the dominant phase, but also considerable hematite present as well as a significant component of magnetite.

We first attempted to reconstruct the film thicknesses using FWDD, which as a reconstruction technique involves filtering to suppress the effects of low-SNR regions of the transfer function as well as to implement a filter specifically designed to pick out features in $r(t)$ that resemble $i(t)$ from the background noise. Due to the fact that FWDD involves filtering, the axial resolution can only be reduced. In this work, FWDD proves unsuccessful in identifying the scale-layer thickness in all cases.

Next, SD based on the iterative-shrinkage algorithm, which provides increased dynamic range as well as superresolution capability in the axial direction, is successful in reconstructing the thickness of the 28.5 μm and 13.4 μm films, but not of the 5.1 μm thick film. SD is limited in differentiating reflected signals that overlap severely in a way also dependent on the dynamic contrast between various reflections in $h(t)$.

Finally, AR was implemented. It improves the accuracy of thickness reconstruction of very thin films by extending the available THz bandwidth through AR extrapolation. In essence, AR exploits techniques developed for time-series prediction, but implemented in the frequency domain. AR proved to provide a reliable thickness measurement for all samples studied, including the thinnest (5 μm). Moreover, unlike techniques limited to a cross section, THz reflectivity measurements can be applied across the entire surface, thus enabling a better exploration of the uniformity of the film.

In summary, THz reflectometry may provide a reliable non-destructive and contactless modality to measure scale film thicknesses on metals down to at ~5 μm, and by extension other electrically non-conducting oxide film thicknesses. THz pulsed techniques for this application proved successful only due to the combined exploitation of the physical measurement technique with the appropriate signal-processing techniques.

CRediT authorship contribution statement

Min Zhai: Investigation, Formal analysis, Software, Writing - original draft.**Alexandre Locquet:**Conceptualization, Methodology, Validation, Writing - review & editing.**Cyrielle Roquelet:**Methodology, Resources.**Patrice Alexandre:**Resources.**Laurence Daheron:** Resources.**D.S. Citrin:**Conceptualization, Supervision, Writing - review & editing.

Declaration of competing interest

The authors declare that they have no known competing financial interests or personal relationships that could have appeared to influence the work reported in this paper.

Acknowledgment

Funding for this work was provided in part by Conseil Régional Grand Est and CPER SusChemProc.

References

[1] K. Darowicki, P. Slepski, M. Szocinski, Application of the dynamic EIS to investigation of transport within organic coating, Prog. Org. Coat. 52 (4) (2005) 306–310, https://doi.org/10.1016/j.porgcoat.2004.06.007.
[2] R.M. Souto, Y. Gonzalez-Garcia, J. Izquierdo, S. Gonzalez, Examination of organic coating on metallic substrates by scanning electrochemical microscopy in feedback mode: revealing the early stages of coating down in corrosive environments, Corros. Sci. 52 (3) (2010) 748–753, https://doi.org/10.1016/j.corsci.2009.10.035.
[3] A. Gallego, J.F. Gil, E. Castro, R. Piotrkowski, Identification of coating damage processes in corroded galvanized steel by acoustic emission wavelet analysis, Surf.

Coat. Technol. 201 (8) (2007) 4743–4756, https://doi.org/10.1016/j.surfcoat.2006.10.018.
[4] Y. He, G.Y. Tian, M. Pan, D. Chen, H. Zhang, An investigation into eddy current pulsed thermography for detection of corrosion blister, Corros. Sci. 78 (2014) 1–6, https://doi.org/10.1016/j.corsci.2013.09.001.
[5] I. Alig, M. Bargmann, H. Oehler, D. Lellinger, M. Wanner, D. Koch, Investigation of delamination mechanisms in polymer coatings by scanning acoustic microscopy, J Phy. D, Appl Phy. 44 (3) (2011) 34009, , https://doi.org/10.1088/0022-3727/44/3/034009.
[6] Y. Watanabe, S. Fujisawa, A. Yonezu, X. Chen, Quantitative evaluation of adhesion quality of surface coating by using pulse laser-induced ultrasonic waves, Surf. Coat. Technol. 286 (2016) 231–238, https://doi.org/10.1016/j.surfcoat.2015.12.026.
[7] N. Hasegawa, T. Nagashma, K. Hirano, Thickness measurement of iron-oxide layers on steel plates using terahertz reflectomery, 2011 International Conference on Infrared, Millimeter, and Terahertz Waves, doi:https://doi.org/10.1109/irmmw-THz.2011.6104964.
[8] J.B. Jackson, J. Bowen, G. Walker, J. Labaune, G. Mourou, M. Menu, K. Fukunaga, A survey of terahertz applications in cultural heritage conservation science, IEEE Trans. Terahertz Sci. Technol. 1 (2016) 220–231, https://doi.org/10.1109/TTHZ.2011.2159538.
[9] D. Crawley, C. Longbottom, V.P. Wallace, B. Cole, D. Arnone, M. Pepper, Three-dimensional terahertz pulse imaging of dental tissue, J. Biomed. Opt. 8 (2) (2003) 303–307, https://doi.org/10.1117/1.1559059.
[10] K. Su, Y.C. Shen, J.A. Zeitler, Terahertz sensor for non-contact thickness and quality measurement of automobile paints of varying complexity, IEEE Trans. Terahertz Sci. Technol. 4 (4) (2014) 432–439, https://doi.org/10.1109/TTHZ.2014.2325393.
[11] Z.Y. Wang, Y.H. Han, N.N. Xu, L. Chen, C.W. Li, L. Wu, W.L. Zhang, Characterization of thin metal films using terahertz spectroscopy, IEEE Trans. Terahertz Sci. Technol. 8 (2) (2018) 161–164, https://doi.org/10.1109/TTHZ.2017.2786692.
[12] M. Zhai, A. Locquet, C. Roquelet, D.S. Citrin, Terahertz non-destructive thickness characterization of optically thin scale layers on steel, 44th International Conference on Infrared, Millimeter, and Terahertz Waves, 2019, https://doi.org/10.1109/IRMMW-THz.2019.8874181.
[13] R. Neelamani, H. Choi, R. Baranuik, ForwaRD: Fourier-wavelet regularized deconvolution for ill-conditioned systems, IEEE Trans. Signal Processing 52 (2) (2004) 418–433, https://doi.org/10.1109/TSP.2003.821103.
[14] G.C. Walker, J.W. Bowen, J. Labaune, J.B. Jackson, S. Hadjiloucas, J. Roberts, G. Mourou, M. Menu, Terahertz deconvolution, Opt. Expr. 20 (25) (2012) 27230–27241, https://doi.org/10.1364/OE.20.027230.
[15] Y. Chen, S.Y. Huang, E. Pickwell-MacPherson, Frequency-wavelet domain deconvolution for terahertz reflection imaging and spectroscopy, Opt. Expr. 18 (2) (2010) 1177–1190, https://doi.org/10.1364/OE.18.001177.
[16] N. Palka, R. Panowicz, M. Chalimoniuk, R. Beigang, Non-destructive evaluation of puncture region in polyethylene composite by terahertz and x-ray radiation, Composites B Eng 92 (2016) 315–325, https://doi.org/10.1016/j.compositesb.2016.02.030.
[17] G.M. Zhang, C.Z. Zhang, D.M. Harvey, Sparse signal representation and its applications in ultrasonic NDE, Ultrasonics 52 (3) (2012) 351–363, https://doi.org/10.1016/j.ultras.2011.10.001.
[18] E.P.J. Parrott, S.M.Y. Sy, T. Blu, V.P. Wallace, E. Pickwell-MacPherson, Terahertz pulsed imaging in vivo: measurements and processing methods, J. Biomed. Opt. 16 (10) (2011) 106010–106018, https://doi.org/10.1117/1.3642002.
[19] J. Dong, A. Locquet, D.S. Citrin, Terahertz super-resolution stratigraphic characterization of multilayered structures using sparse deconvolution, IEEE Trans. Terahertz Sci. Technol. 7 (3) (2017) 260–267, https://doi.org/10.1109/TTHZ.2017.2673542.
[20] F. Schrettle, C. Kant, P. Lunkenheimer, F. Mayr, J. Deisenhofer, A. Loidl, Wüstite: electric, thermodynamic and optical properties of FeO, Eur Phy J B 85 (5) (2012) 164, https://doi.org/10.1140/epjb/e2012-30201-5.
[21] M. Takeda, T. Onishi, S. Nakakubo, S. Fujimoto, Physical properties of iron-oxide scales on Si-containing steels at high temperature, Mater. Trans. 50 (9) (2009) 2242–2246, https://doi.org/10.2320/matertrans.M2009097.
[22] T. Henning, V.B. Il'in, N.A. Krivova, B. Michel, N.V. Voshchinnikov, WWW database of optical constants for astronomy, Astron. Astrophys. Suppl. Ser. 136 (1999) 405–406, https://doi.org/10.1051/aas:1999222.
[23] T. Henning, B. Begemann, H. Mutschke, J. Dorschner, Optical properties of oxide dust grains, Astron. Astrophys. Suppl. Ser. 112 (1995) 143–149.
[24] T.R. Steyer, Infrared Optical Properties of Some Solids of Possible Interest in Astronomy and Atmospheric Physics, Ph.D. Thesis University of Arizona, United States, 1974.
[25] U. Buchenau, I. Müller, Optical properties of magnetite, Solid State Commun. 11 (1972) 1291–1293, https://doi.org/10.1016/0038-1098(72)90845-9.
[26] See p. 188, D.R. Huffman, Interstellar grains the interaction of light with a small-particle system, Adv. Phys. 26 (1977) 129–230, https://doi.org/10.1080/00018737700101373.
[27] J. Dong, A. Locquet, D.S. Citrin, Enhanced terahertz imaging of small forced delamination in woven glass fibre-reinforced composites with wavelet de-noising, J. Infrared Milli. Terahz. Waves 37 (2016) 289–301, https://doi.org/10.1007/s10762-015-0226-9.
[28] J. Dong, A. Locquet, D.S. Citrin, Terahertz quantitative nondestructive evaluation of failure modes in polymer-coating steel, IEEE J. Quantum Electron. 23 (4) (2017) 1–7, https://doi.org/10.1109/JSTQE.2016.2611592.
[29] L. Wei, Z. Huang, Q. Wen, Sparse deconvolution method for improving the time-resolution of ultrasonic NDE signals, NDT&E Int 42 (5) (2009) 430–434, https://doi.org/10.1016/j.ndteint.2009.01.009.
[30] J. Dong, B. Kim, A. Locquet, P. McKeon, N. Declercq, D.S. Citrin, Nondestructive evaluation of forced delamination in glass fiber-reinforced composites by terahertz and ultrasonic waves, Compos. Part B Eng. 79 (2015) 667–675, https://doi.org/10.1016/j.compositesb.2015.05.028.
[31] S. Zhou, D.G. Valchev, A. Dinovitser, J.M. Chappell, A. Iqbal, B.W. Ng, T.W. Kee, D. Abbott, Terahertz signal classification based on geometric algebra, IEEE Trans. Terahertz Sci. Technol. 6 (6) (2016) 793–802, https://doi.org/10.1109/TTHZ.2016.2610759.
[32] L. Lines, T. Ulrych, The old and the new in seismic deconvolution and wavelet estimation, Geophys. Prospect. 25 (3) (1977) 512–540, https://doi.org/10.1111/j.1365-2478.1977.tb01185.x.
[33] J. Dong, A. Locquet, D.S. Citrin, Depth resolution enhancement of terahertz deconvolution by autoregressive spectral extrapolation, Opt. Lett. 42 (9) (2017) 1828–1831, https://doi.org/10.1364/OL.42.001828.